Multistage laser shock improves surface structural properties of aluminum alloy

Xiaohan Zhang[a], Min Xia[c], Chen Zhang[a,*], Yaowu Hu[a,b,*]

[a]The Institute of Technological Sciences, Wuhan University, Wuhan, 430072, China
[b]School of Power and Mechanical Engineering, Wuhan University, Wuhan, 430072, China
[c]Department of Engineering, Lancaster University, Lancaster, LA1 4YW, United Kingdom
*Corresponding author: Yaowu Hu
E-mail: yaowuhu@whu.edu.cn
*Corresponding author: Chen Zhang
E-mail: c.zhang@whu.edu.cn

Abstract

Functional thin-walled aluminum alloys were the main production materials for the outer wall of novel lightweight flight power. The harsh service conditions of power had put forward strict requirements on the mechanical properties and functional characteristics of thin-walled parts. The functional surface produced by the traditional process was difficult to overcome the functional-mechanical properties trade-off. The feasibility and productivity of complex curved components was another issue. How to efficiently manufacture functional structures with excellent mechanical properties was the key technical bottleneck that needed to be broken through in current engineering field. A novel strategy called multistage laser shock peening (MLSP) was proposed to manufacture microstructures with functional and excellent mechanical properties. The mechanical properties, surface wettability, electrochemical behavior and tribological behavior of MLSP samples were systematically discussed and analyzed. A series of micro-pits filled with abundant micro and nano structures were shown on the surface of the enhanced MLSP sample, which constituted functional microstructures across scales. Due to the decrease of the shock pressure, the hardness of the material presented a gradient distribution in the horizontal and vertical directions. Effective synergistic plastic deformation was achieved in MLSP-induced multistage heterogeneous gradient structures, which increased the yield strength of the material by 214 % from 21 MPa to 66 MPa while the ductility was slightly reduced from 26 % to 25 %. Compared with the traditional laser shock technology, the MLSP samples had more balanced structural properties. MLSP strategy could provide a new way to manufacture high reliability functional metal surfaces.

Key words: Multistage laser shock peening; Heterogeneous structure; Micro-pits; Functional surface; Mechanical properties

1. Introduction

Lightweight aluminum alloy with excellent thermal conductivity has become the preferred material for new thin-walled key components of flight power [1–5]. The complex service environment of flight power, such as high cold, humidity, high-speed particle erosion, etc., puts forward more stringent requirements on the functional characteristics of the outer wall of the aircraft, such as hydrophobicity, corrosion resistance and wear resistance. The microstructure of the metal surface is the direct source of the functional properties of the material, but the unsatisfactory mechanical properties of the microstructure often become the main cause of the attenuation of the functional properties of the material, which seriously affects the efficiency and reliability of the aircraft operation [6,7]. Therefore, how to fabricate a metal wall material with both excellent mechanical properties and functional properties has become the main technical bottleneck that needs to be solved urgently.

Common fabrication methods for metal surface microstructures include electrochemical corrosion [8–10], vapor deposition [11–13], electrical discharge machining [14–16], shot peening [17–19]. However, these traditional manufacturing methods all have this unavoidable process shortcoming. The processing quality of electrochemical corrosion is difficult to control effectively. Vapor deposition has higher processing quality, but lower processing

efficiency and less flexibility. The material has thermal defects that are difficult to remove after electrical discharge machining. While shot peening enables the fabrication of large-area microstructures, the machining accuracy is low due to the random shot blasting. Compared with the conventional process methods, laser processing technology has the advantages of environmental friendliness, high flexibility and strong controllability [20,21]. The plasma shock wave induced by pulse laser can generate rich micro-nano morphology on the metal surface, and can produce excellent strengthening effect on the metal [22,23]. Therefore, pulse laser fabrication is considered to be an effective method to fabricate high-reliability microstructures. The direct ablation of femtosecond pulsed laser can realize the fabrication of micro-nano topography with controllable size on the surface of the material under the premise of the minimum heat-affected zone. However, low manufacturing efficiency and high equipment cost are undoubtedly the Achilles' heel of femtosecond laser manufacturing [24].

Nanosecond pulsed lasers can greatly improve the manufacturing efficiency of microstructures, such as nanosecond laser direct ablation and laser shock imprinting with molds. For instance, Ding et al. [25] used a high-energy nanosecond pulsed laser to directly ablate metal surfaces immersed in water, and achieved the fabrication of cross-scale hydrophobic metal surfaces with the help of chlorosilane low-surface-energy reagents. Trdan et al. [26] studied the tribological properties of aluminum alloy manufactured by laser shock without coating, and found that the microstructure morphology of the surface induced by pulse laser has a positive impact on the friction and wear properties of the material. Wang et al. [27] studied the tribological properties of NiTi alloy produced by laser shock without coating, and found that the remelting layer produced by laser ablation improved the wear resistance of the material. Kaufman et al. [28] found that compared with laser shock with coating, the intergranular corrosion rate of samples manufactured by laser shock without coating was significantly reduced. However, the morphology transition of direct ablation by nanosecond lasers in the traditional sense depends on the spot size. Large area laser direct ablation would increase the brittleness of the material and affect the mechanical properties. Laser shock imprinting with a mold is another way to increase manufacturing efficiency. Li et al. [29] used a micro-mold with a rough concave texture to process a multi-scale surface microstructure under the action of a laser shock wave, thereby realizing the control of the wettability of the material surface. However, the samples manufactured by the above process method have a single surface morphology, which cannot realize the collection of many functional characteristics. The manufacturing cost of the mold, the reduction of the peak energy of the pressure wave after passing through the mold, and the inability to face complex curved structures are another issue that needs to be considered.

Machining the surface into a heterogeneous structure was expected to achieve excellent mechanical properties. By using optical mask or spatial light modulator, the laser beam could be separated and the shock pressure on the material surface could be heterogeneous. Lechthaler et al. [30] used a device combining imaging and two-beam interference to perform beam shaping of nanosecond lasers, thereby obtaining a spot with a uniform energy density distribution. Dai et al. [31] used optical mask laser shock processing technology to fabricate micro-dimple arrays on the surface of LY2 aluminum alloy. Ye et al. [32] used laser shock assisted direct imprinting method to produce patterned micro-indentations on the surface of NiTi shape memory alloy. However, the process used a carbon layer as a sacrificial layer, so no visible microstructure could be created on the surface of the material. When BK7 glass was taken as the confinement layer, there was a blind area of confinement, that was, plastic deformation occurred only in the direction of the thickness of the metal mesh, and the surface of the material not covered by the metal mesh was still not enhanced. The morphology of the metal surface produced by the existing process is mostly concentrated in a single scale, and there is an unstrengthened area, which belongs to selective laser shock strengthening, and the unstrengthened area becomes a high-risk area of failure. In addition, the existing work do not systematically explain or even ignore the improvement mechanism of the mechanical properties of the microstructure. Therefore, how to design a multistage enhanced and highly reliable functional microstructure has become a key problem that needs to be solved urgently.

This paper aims to solve the problem that the inability of existing processes to fabricate metal surfaces that combine functionality and excellent mechanical properties at large scale. Multistage laser shock peening (MLSP) method was proposed to fabricate a cross-scale functional surface structure with excellent mechanical properties on the metal surface. The mechanical properties and functional properties of MLSP, all laser shock peening (ALSP) and no laser shock

peening (NLSP) samples were discussed and analyzed. In addition, the enhanced mechanism of their mechanical properties and the origin of the functional properties of the MLSP samples were also revealed.

2. Materials and methods

2.1. Materials

The 7075 aluminum alloy was selected for MLSP process. The thickness of the aluminum alloy plate was 200 μm. The main element composition of the aluminum alloy plate is shown in **Table 1**. Before laser shock, the samples were annealed in a tube furnace. The annealing atmosphere was vacuum environment, the annealing temperature was 370 ℃, and annealing time was 2 h. As shown in **Fig.S1**, the 316 stainless steel metallic mesh of three different sizes were used as assistant structure of the MLSP, acting as optical masks and momentum transmission layers. The main element composition of the thin metallic mesh is shown in **Table 2**. The mesh size of the thin metallic mesh (a*b) and the thickness (d) of the thin metal mesh are shown in **Table 3**.

Table. 1 Main element composition of the 7075 aluminum alloy

Element	**Si**	**Fe**	**Cu**	**Bi**	**Mg**	**Ni**	**Cr**	**Zn**	**Ti**	**Al**
Content (*wt*%)	0.31	0.35	1.66	0.20	2.61	-	0.23	5.60	0.10	Bal

Table. 2 Main element composition of the thin metallic mesh

Element	**C**	**Mn**	**P**	**S**	**Si**	**Cr**	**Ni**	**Mo**	**N**	**Al**
Content (*wt*%)	0.03	2	0.03	0.02	0.75	16.75	13.25	2.45	0.16	Bal

Table. 3 Geometric parameters of the thin metallic mesh

Serial number	**a×b (μm^2)**	**d (μm)**
Case 1	100×100	50
Case 2	150×225	70
Case 3	250×425	80

2.2. Processing setup

Fig. 1 shows the schematic diagram of MLSP process. Nanosecond pulse laser with adjustable pulse energy was used to execute MLSP process. The process parameters of MLSP are shown in **Table 4**. As shown in **Fig. 1** (a), the aluminum alloy with the thin metallic mesh on the surface was placed in the center of the liquid pool. The pulsed laser was vertically injected into deionized water through a mirror and a focusing lens. Part of the laser beam directly acted on the surface of the target material through the thin metallic mesh. Another part of the laser beam acted on the surface of the metallic mesh. The air blowing device was used to change the path of the splashed droplets to prevent contamination of the lens group and influence the beam quality. The three-axis mobile platform drove the movement of the samples. High speed camera was used to capture the real-time picture of MLSP process. **Fig. 1** (b) shows the concept of multistage laser shock. Plasma would be generated when pulsed laser interacted with metal mesh and sample. As a confinement layer, deionized water could completely fill the surface of metallic mesh and sample, and there was no obvious confinement blind area. Therefore, shock waves would be generated on the surface of the metallic mesh and the sample. The shock wave generated by the direct interaction between the laser and the material was the first stage shock wave. The shock wave transmitted to the sample surface through the metallic mesh was the second stage shock wave. MLSP could induce the surface structure shown in **Fig. 1** (c), which would be described in detail in Section 3.1. As shown in **Fig. 1** (d), the real-time image of MLSP process would be described in detail in Section 4.1.

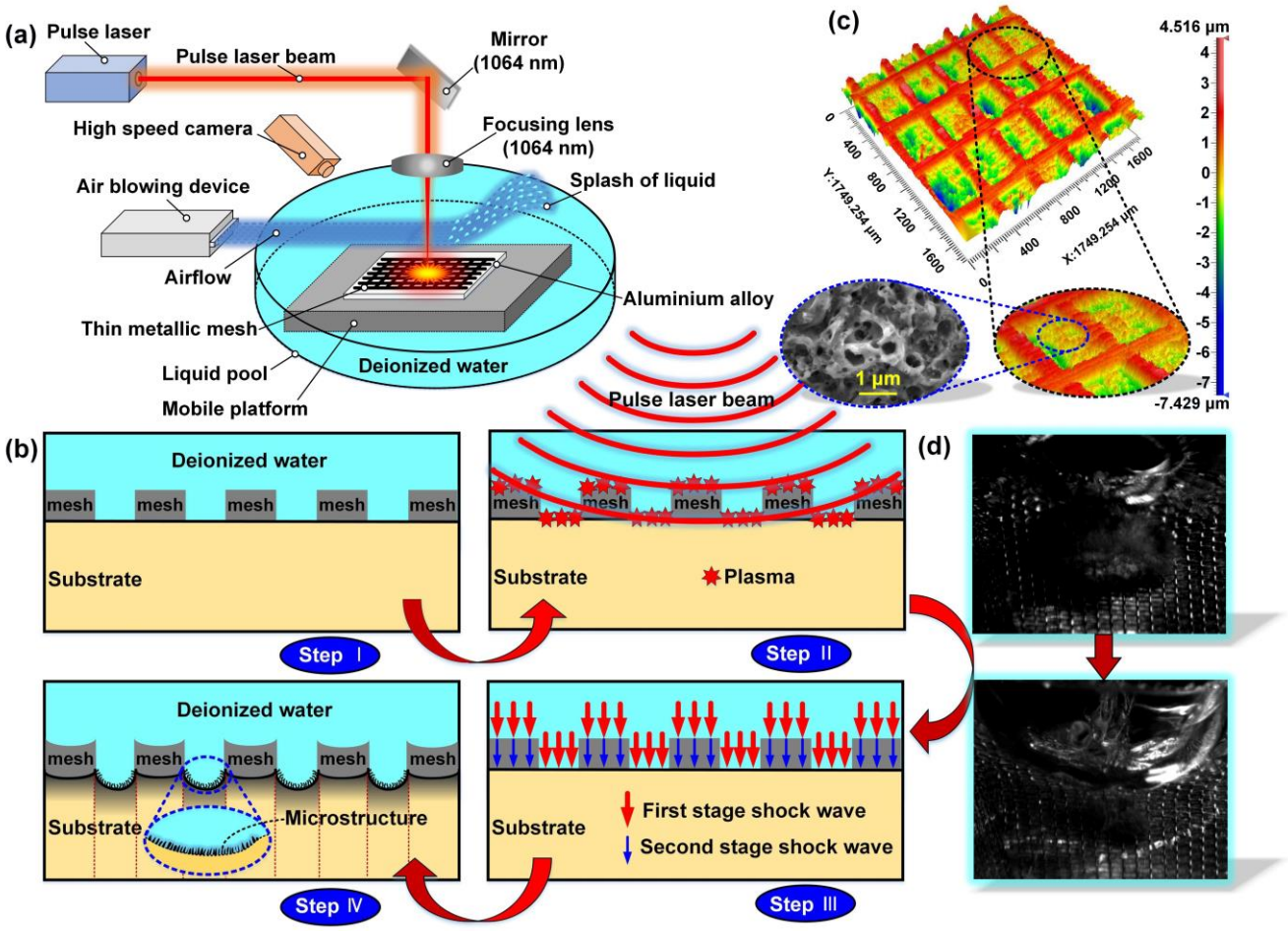

Fig. 1. Schematic diagram of the process of MLSP: (a) device schematic, (b) concept of multistage laser shock, (b) MLSP induced microstructure, (d) real time image of MLSP process.

Table. 4 Process parameters of the MLSP

Process parameters	value
Laser wavelength	1064 nm
Laser pulse width	7 ns
Spot size	1.5 mm
Laser pulse frequency	6 Hz
Single pulse energy	1 J
Overlap rate of the laser spot	50%
Confinement layer	Deionized water
Confinement layer	5 mm

2.3. Characterisation methods

The optical microscope (BX53M, Olympus Inc., Japan) was used to observe the macroscopic appearance of the metallic mesh. The white light interferometric 3D profiler (NewViewTM 9000, ZYGO Inc., USA) was used to measure the surface topography and roughness. The field emission scanning electron microscope (MIRA 3, TESCAN Brno,s.r.o. Inc., Czech Republic) with energy dispersive spectrometer (EDS) (Aztec Energy, Oxford Instruments Nanoanalysis Inc., UK) was used to observe the microscopic morphology and element content of the sample. The high-speed camera (Phantom, V1612, USA) matched with a miniature zoom lens (Navitar 12-X) was used to film the MLSP and NLSP processes. The nanoindenter (TI 950 Tribolndenter^{TM}, Bruker Inc., USA) was used to test the hardness distribution of the sample. The pressure load was 10 mN, and the holding time was 2 s. The universal testing machine (5956, Instron Inc., USA) was used to test the tensile properties of the sample. The tensile tests were carried out three times at room

temperature at the tensile rate of 2 mm/min for each process. The size parameters of the tensile sample were as follows: the parallel length was 34.6 mm, the width was 6 mm, the radius of the transition fillet was 20 mm, and the thickness was 0.2 mm (The detailed size and laser scanning path of the tensile sample are shown in **Fig. S2**). The X-ray diffractometer (XRD) (X' Pert PRO, Almelo, Netherlands) was was used to perform phase analysis and assess residual stress trends. The goniometry instrument (JCY-4, Fangrui Inc., China) was used to measure the contact angle of the sample at room temperature (25± 2 ℃) with a 4 μL distilled water droplet. A multi-channel electrochemical workstation (Ivium-n-Stat, Ivium technologies BV Inc., Netherlands) was used to carry out the electrochemical corrosion experiments. The corrosion solution was 3.5wt% sodium chloride solution, and the reference electrode was AgCl. The scanning rate of the polarization curve experiment was 10 mV/s, and the scanning range was -2~2 V. With the aid of friction and universal tribometer (MFT-5000, Rtec Instruments, Inc., USA), and using 440C steel dual balls with a diameter of 6.350 mm, lubrication friction experiments at room temperature were carried out. Shell Helix HX3 15X-40 lubricating oil was used as the lubricating medium.

2.4. Numerical simulation

The finite element model of uniaxial tension of samples with different structure was established based on the ductile damage model. The simulation results of uniaxial tension provided theoretical support for the tensile property gain mechanism of MLSP samples. In addition, numerical models of MLSP and ALSP processes were established based on the Johnson-cook model to obtain the residual stress distribution on the surface of samples with different mesh sizes and without mesh. The calculation results of residual stress could provide theoretical support for the improvement of mechanical strength of materials. Finite element calculations were performed on a workstation with i7-10700CPU@2.90GHz processor and 32GB (RAM) running memory (More modeling details can be found in **Section 8-9** of **Supplementary Materials**).

3. Results

3.1. Surface topography

The surface morphology had a strong relationship with the functional properties of materials (such as hydrophobicity, corrosion resistance, wear and friction resistance, etc.) [33–35] Here, the surface morphology of samples manufactured under different processes was discussed, and the correlation between process parameters and surface morphology was established.

Fig. 2 shows the morphology of samples produced by different processes. Observing and comparing **Fig. 2** (a)-(e) (the laser scanning path was shown by the blue arrow), the surface roughness (Sa) of samples produced by different processes was different. Compared with the NLSP sample, laser shock could significantly improve the roughness of the material surface. With the increase of the mesh size of the metallic mesh, the surface roughness of the sample increased gradually. The 2D profile of the sample could further reflect the change in the roughness and depth of structure of the sample as shown in **Fig. 2** (f). MLSP could induce fluctuations of about 3 μm-7 μm on the material surface. In addition, the rising mesh size of the metallic mesh increased the deformation amount of the material surface, which undoubtedly became another significant factor for the improvement of the roughness of the sample. MLSP produced a series of micro pits with array distribution on the sample surface. The micro-pits was non-uniform and its bottom was tapered, which could be attributed to the gradual decrease of the peak energy of the shock wave during the transfer process. Observing **Fig. 2** (g)-(i), abundant microstructures were distributed in the micro-pits with array distribution, and these structures were spherical, grooved and microporous. The micro-pits made by MLSP could effectively protect the microstructure in the pits. The MLSP process could effectively control the functionality of the sample surface by adjusting the geometric size of the micro-pits. The relationship between the surface morphology of metals and their functional properties would be highlighted in Section 3.3.

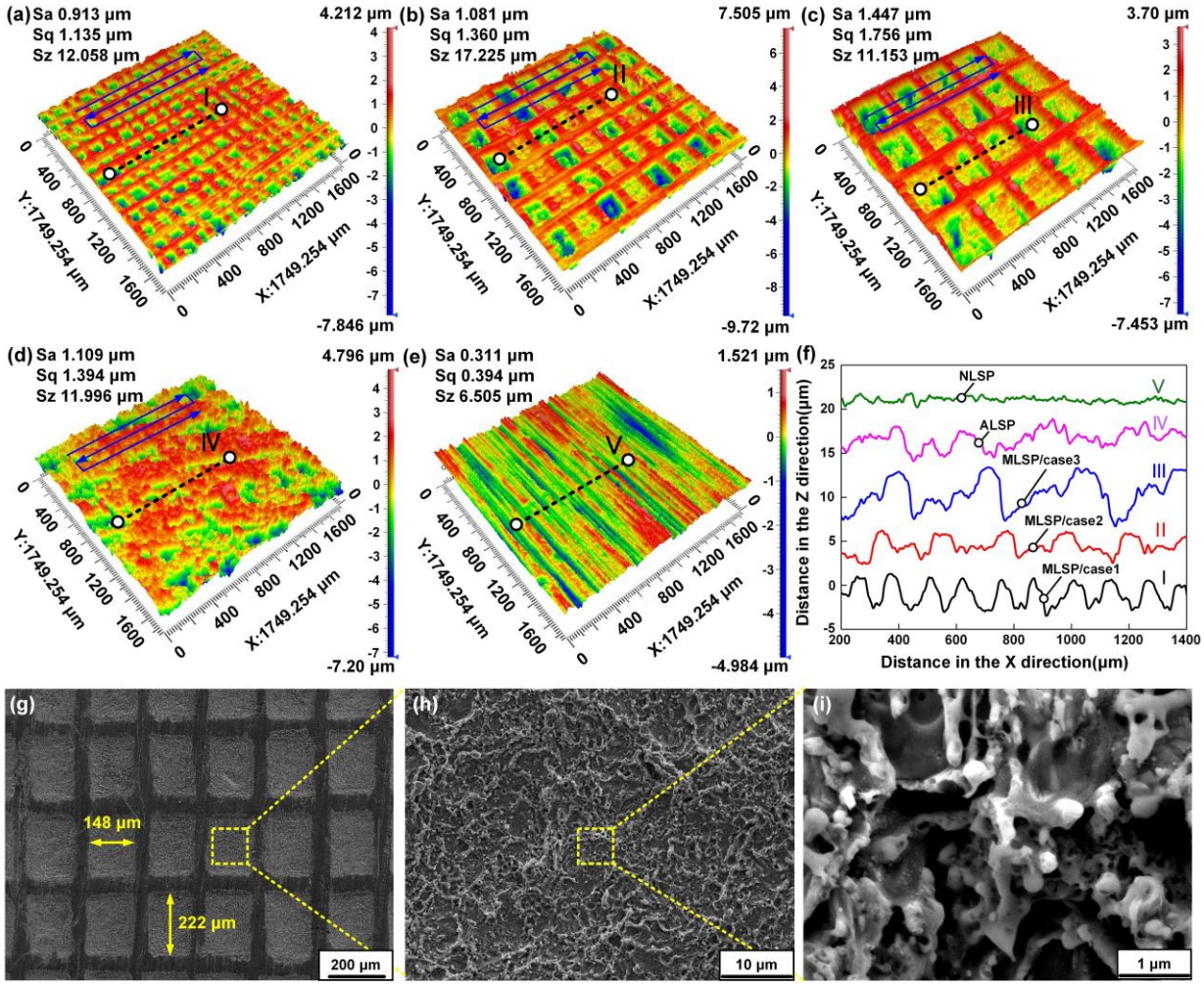

Fig. 2. Morphology of samples produced by different processes: (a) 3D profile/MLSP/case1, (b) 3D profile/MLSP/case2, (c) 3D profile/MLSP/case3, (d) 3D profile/ALSP, (e) 3D profile/NLSP, (f) 2D profile of the dashed cross-sections in (a)-(e), (g) SEM image/MLSP/case2, (h) partial enlarged view of (g), (i) partial enlarged view of (h).

3.2. Mechanical properties

The mechanical properties of surface structure were the key factors affecting its service life. In this section, the mechanical properties of samples manufactured by different processes were evaluated by nanoindentation tests and tensile tests. The relationship between processing conditions and mechanical properties of samples was established.

Fig. 3 (a) shows the hardness distribution in the thickness direction of samples manufactured by different processes. The laser shock caused a gradient distribution of hardness in the vertical direction of the material. In contrast, MSLP/case3 samples and ALSP samples had similar hardness distributions at the same thickness. As the size of the metal mesh decreases, the hardness of the sample decreased at the same thickness. **Fig. 3** (b) shows the hardness distribution in the horizontal direction of the MLSP sample. The hardness of the substrate directly interacting with the pulse laser was higher than that of the substrate covered by the metallic mesh. The hardness of the material area with and without metal mesh showed a gradient change. As the mesh size increases, the hardness of the material covered by the metallic mesh, and the hardness of the material directly interacting with the laser increased gradually. The displacement-load curves in the nanoindentation test were shown in **Fig. S3**. MLSP could obtain a mutistage heterogeneous structure with gradient changes of hardness in the horizontal and vertical direction of the material, which was different from the single gradient structure produced by traditional laser shock process [36,37]. **Fig. 3** (c) shows the tensile properties of samples under different processes. The NLSP samples had low yield strength (~21 Mpa) but high ductility (~26 %). Compared with the NLSP samples, the yield strength of the ALSP samples was increased to ~89 MPa, but the ductility was greatly reduced to ~9 %. The strength and ductility of the MLSP samples were between those of

NLSP and ALSP. With the increase of the mesh size of the metallic mesh, the yield strength of the sample increased from 66 MPa of case1 to 77 MPa of case3, the ductility of the sample decreased from ~25% of case1 to ~21 % to case3. The detailed stress-strain curve is shown in **Fig. S4**. The fracture morphology of the tensile sample could laterally reflect the strength and ductility of the material. Observing and comparing **Fig. 3** (d)-(h), the ALSP samples showed typical intergranular brittle fracture morphology. The tensile fracture of the NLSP sample was composed of many honeycomb-like tiny pits. These craters were actually grown hollow cores. The dimples were staggered and stacked together to form a dimple group, showing a typical high-energy absorption ductile fracture morphology. The size and number of dimples were closely related to the ductility of the material. With the increase of the mesh size of the metallic mesh, the size and number of the dimples in the tensile fracture of the samples fabricated by the MLSP process decreased to varying degrees, which was undoubtedly consistent with the tensile test results. The flattening of the tensile fracture was attributed to the residual compressive stress induced by the laser shock (**Fig. 3** (i)).

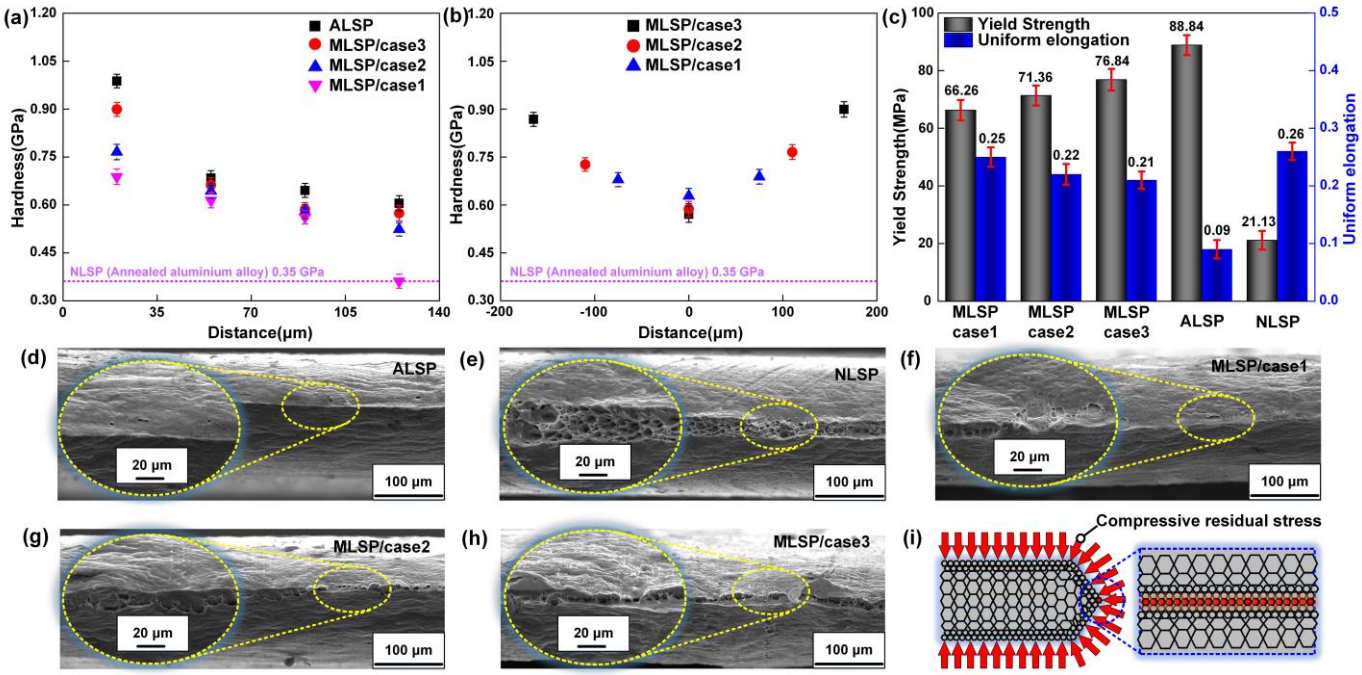

Fig. 3. Hardness and tensile properties of samples manufactured by different processes (test point is located on the cross section of the sample): (a) hardness distribution in vertical direction, (b) hardness distribution in horizontal direction, (c) yield strength and uniform elongation, (d) tensile fracture morphology/ALSP, (e) tensile fracture morphology/NLSP, (f) tensile fracture morphology/case1, (g) tensile fracture morphology/case2, (h) tensile fracture morphology/case3, (i) schematic diagram of the flat tensile fracture morphology.

3.3. Functional properties

In this section, the surface wettability, corrosion behavior and tribological behavior of samples manufactured by different processes were discussed. The relationship between machining conditions and surface functionality was established.

3.3.1. Hydrophobic properties

Surface morphology and surface energy were two crucial factors that affect the wettability of materials [38,39]. The surface morphology of samples was fabricated by laser shock processing. After laser shock, the samples were cleaned with the aid of acetone and an ultrasonic cleaner. Samples produced by different processes were immersed in an ethanol solution containing 1.5% volume percent of chlorosilane reagent [CF3(CF2)5(CH2)2SiCl3] for 4 h 30 min at room temperature. Then the samples were dried by means of a vacuum oven with the temperature of 80 ℃ and the holding time of 1 h. With the aid of chemical reagents, the low surface energy state of the sample surface was realized. **Fig. 4** shows the contact angle of samples under different processes. After coating with low surface energy reagents, all samples showed a hydrophobic state. The contact angle of the MLSP sample was the largest, followed by the ALSP sample, and

the contact angle of the NLSP sample was the smallest. For the MLSP sample, with the increase of the mesh size of the metallic mesh, the contact angle of the sample increased from ~143° to ~153°.

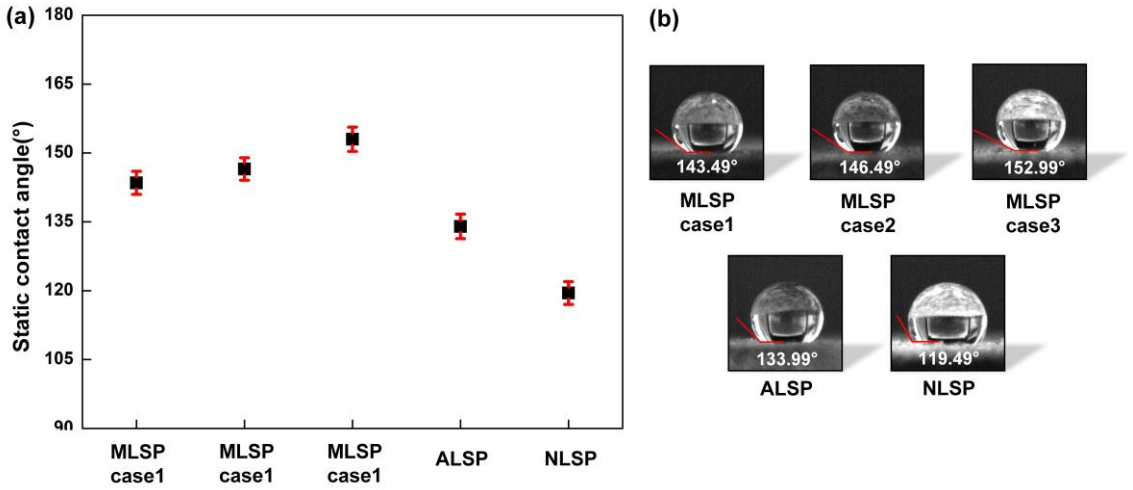

Fig. 4. Hydrophobic properties of samples under different processes: (a) value of static contact angle, (b) real time image of wettability.

3.3.2. Electrochemical behavior

The electrochemical behavior of samples manufactured by different processes in the corrosive environment was tested through electrochemical experiments (**Fig. 5** (a)). **Fig. 5** (b) shows the polarization curves of samples. The polarization curves decreased in the range of 1.5~2.0 V, which was attributed to the different degrees of passivation of the aluminum alloy samples. According to the polarization curve, the self-corrosion potential (**Fig. 5** (c)) and the self-corrosion current density (**Fig. 5** (d)) of the samples produced under different processes were calculated by Tafel extrapolation. Laser shock could make the self-corrosion voltage of the material shift forward. When the self-corrosion voltage was shifted positively, the corrosion resistance of the material became better, but the self-corrosion voltage could only characterize the tendency of the material to corrode. The corrosion current density was proportional to the corrosion rate of the target material, which could more truly characterize the corrosion resistance of the material. The corrosion current density of the NLSP sample was the largest, followed by the MLSP sample, and the ALSP sample was the smallest. With the increase of the mesh size of the metal mesh, the area directly irradiated by the laser beam increased, and the self etching current density of the sample decreased. **Fig. 5** (e)-(i) shows the optical images of corrosion morphology (the laser scanning path was shown by the white arrow). For the NLSP sample, after the corrosion treatment, a large area of corrosion morphology was produced. The corrosion morphology was only observed in the non-laser shock area of the MLSP sample, and the corrosion area decreased with the increase of the mesh size. No obvious corrosion morphology was observed for the ALSP sample. The optical images of corrosion morphology were consistent with the results of Tafel extrapolation.

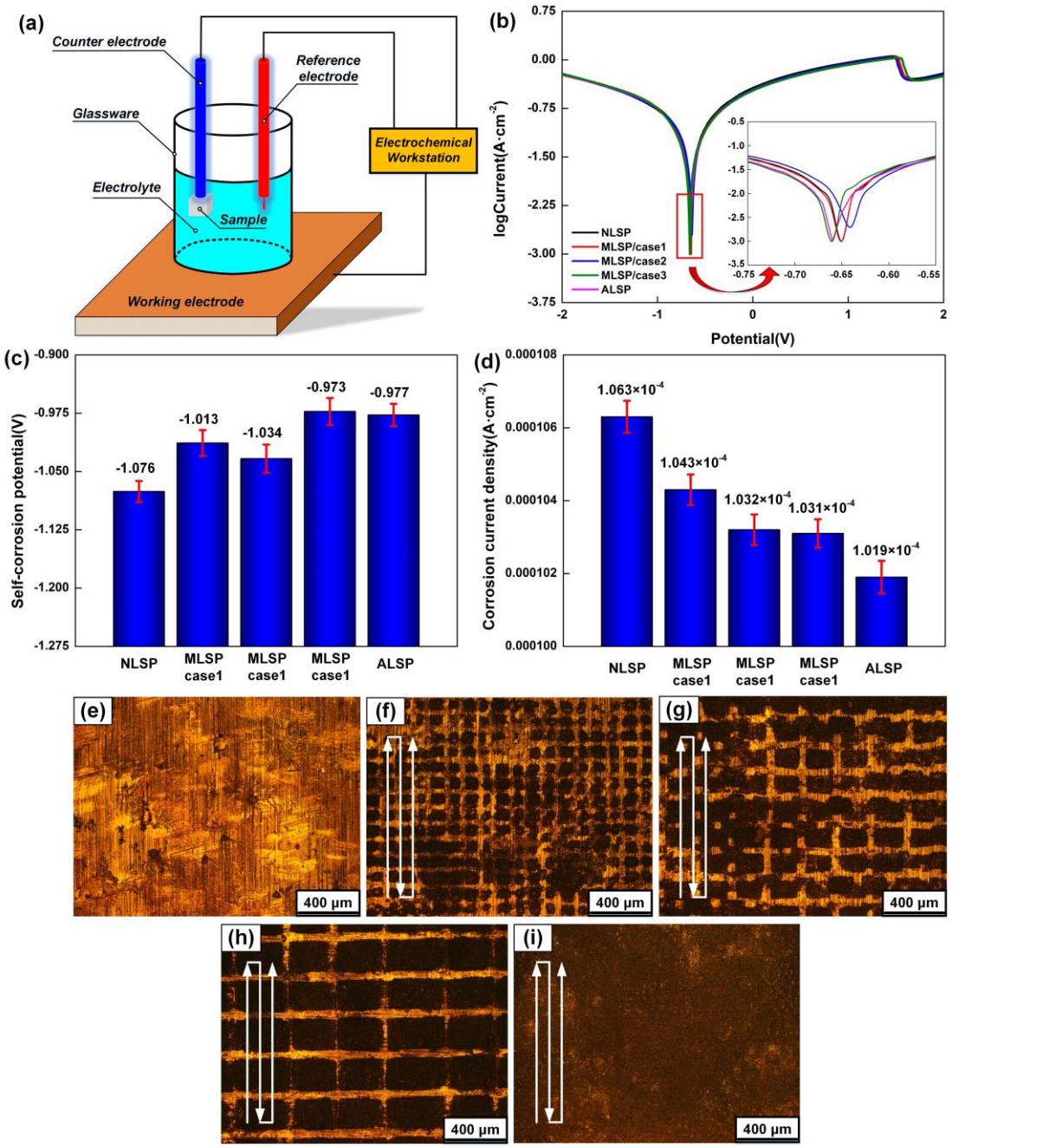

Fig. 5. Electrochemical behavior of samples produced by different processes: (a) electrochemical corrosion experimental device diagram, (b) polarization curves, (c) self-corrosion potential, (d) self-corrosion current density, (e) corrosion morphology/NLSP, (f) corrosion morphology/case1, (g) corrosion morphology/case2, (h) corrosion morphology/case3, (i) corrosion morphology/ALSP.

3.3.3. Tribological properties

The tribological properties of the samples manufactured by different processes were tested through friction and wear experiments (**Fig. 6** (a)). **Fig. 6** (b) shows the friction coefficient of samples. The friction coefficient of the sample had experienced the change process of disorder (0-2.5 s), asymptotic order (~2.5-32.5 s), and order (~32.5-60 s), which undoubtedly corresponded to the process of friction experiment from disorder to gradual order. The friction coefficient of the NLSP sample was the highest, followed by the MLSP sample, and the ALSP sample was the smallest (**Fig. 6** (c)). By analyzing the wear morphology of the samples (**Fig. 6** (d)-(i)), the tribological properties of the samples could be more directly reflected.Compared with **Fig. 2** (f), the wear depth of the samples from deep to shallow were NSLP, MLSP and ALSP. For the MLSP sample, with the increase of the mesh size of the metallic mesh, the depth of the wear scar of the sample decreased.

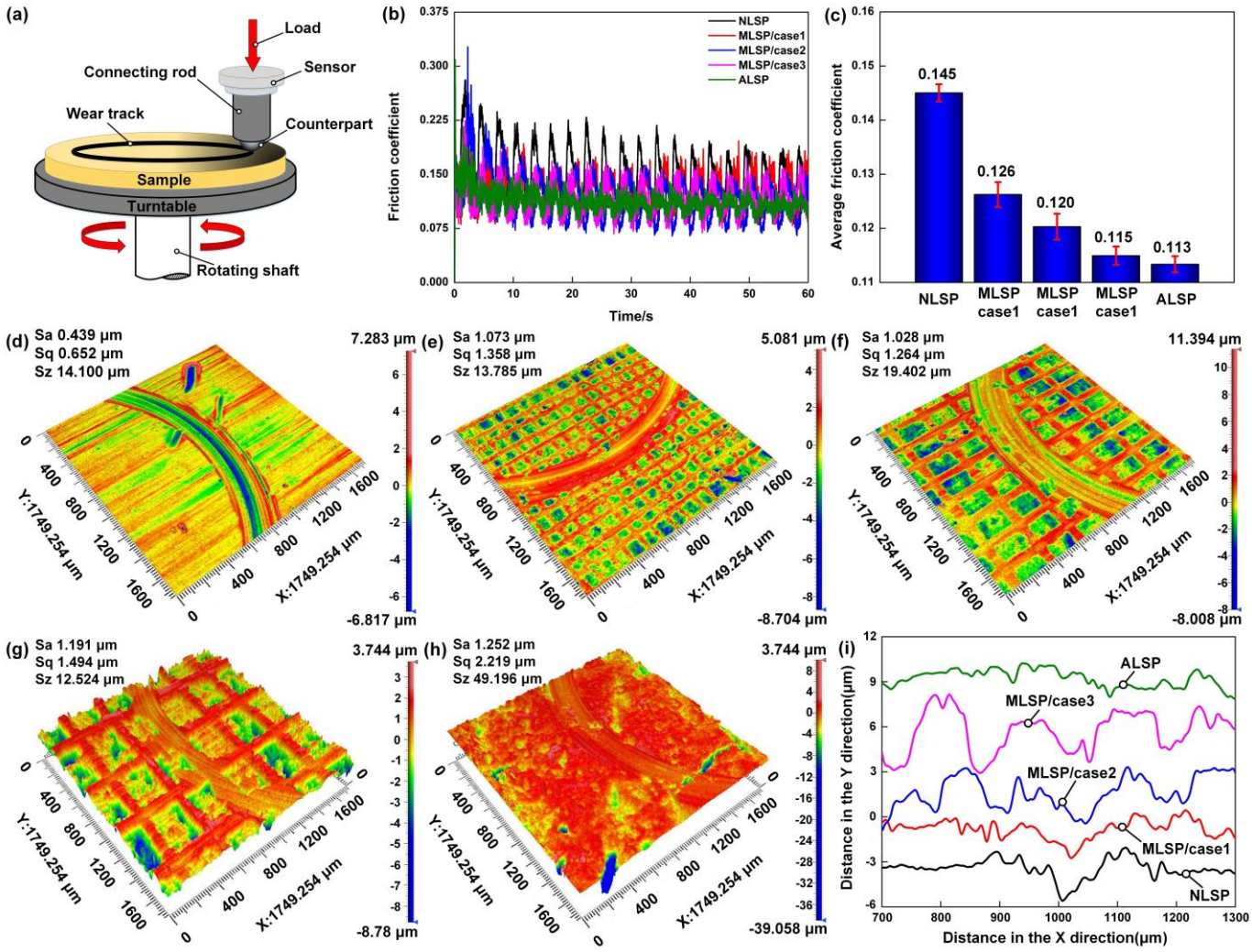

Fig. 6. Tribological properties of samples produced by different processes: (a) friction and wear experimental device diagram, (b) friction coefficient curve, (c) average friction coefficient, (d) 3D profile of wear/NLSP, (e) 3D profile of wear/MLSP/case1, (f) 3D profile of wear/case2, (g) 3D profile of wear/case3, (h) 3D profile of wear/ALSP, (i) 2D profile of wear.

4. Discussions

4.1. Evolution of laser-induced plasma shock waves

Understanding the generation mechanism and propagation process of pressure waves in MLSP process was the premise to analyze the surface topography generation and material mechanical properties response. Here, the generation process of pressure wave in MLSP process was described in detail.

Fig. 7 shows the high-speed images of MLSP. The physical phenomenon of MLSP was similar to that of the conventional LSP (**Fig. S5**). The online monitoring equipment observed that MLSP was accompanied by a series of typical physical phenomena, including the generation-expansion-escape of plasma, the generation-annihilation of reverse jets, microbubbles, and microjets, etc [40–42]. The pulsed laser penetrated the confinement layer material and directly interacted with the surface of aluminum alloy and metallic mesh, inducing a dazzling high-temperature plasma (**Fig. 7** (b)-(c)). At the interface between the confinement layer and the substrate, the plasma induced a bowl-shaped pressure shock wave. Microbubbles and stress wave ripples were observed on the surface of the substrate (**Fig. 7** (d)-(f)). During the time period of t=0-230.76 μs, the volume of the pressure wave interacting with the substrate gradually increased and gradually expanded to the surface of the confinement layer. At the same time, the microbubbles spread from the surface of the substrate to the surface of the constraining layer. During the time period of t=230.76-538.44 μs, as the pressure

wave expanded to the surface of the confinement layer, the volume of the pressure wave interacting with the substrate gradually decreased. At the same time, the laser-induced bubbles also undergone an initiation-expansion-annihilation process. Compared with the bubbles far from the substrate, the size of the bubbles close to the substrate was larger, which was because the bubbles continue to split and expand from bottom to top. As the pressure wave spreads, many fine bubble groups remained and oscillated on the surface of the substrate (**Fig. 7** (i)-(o)).

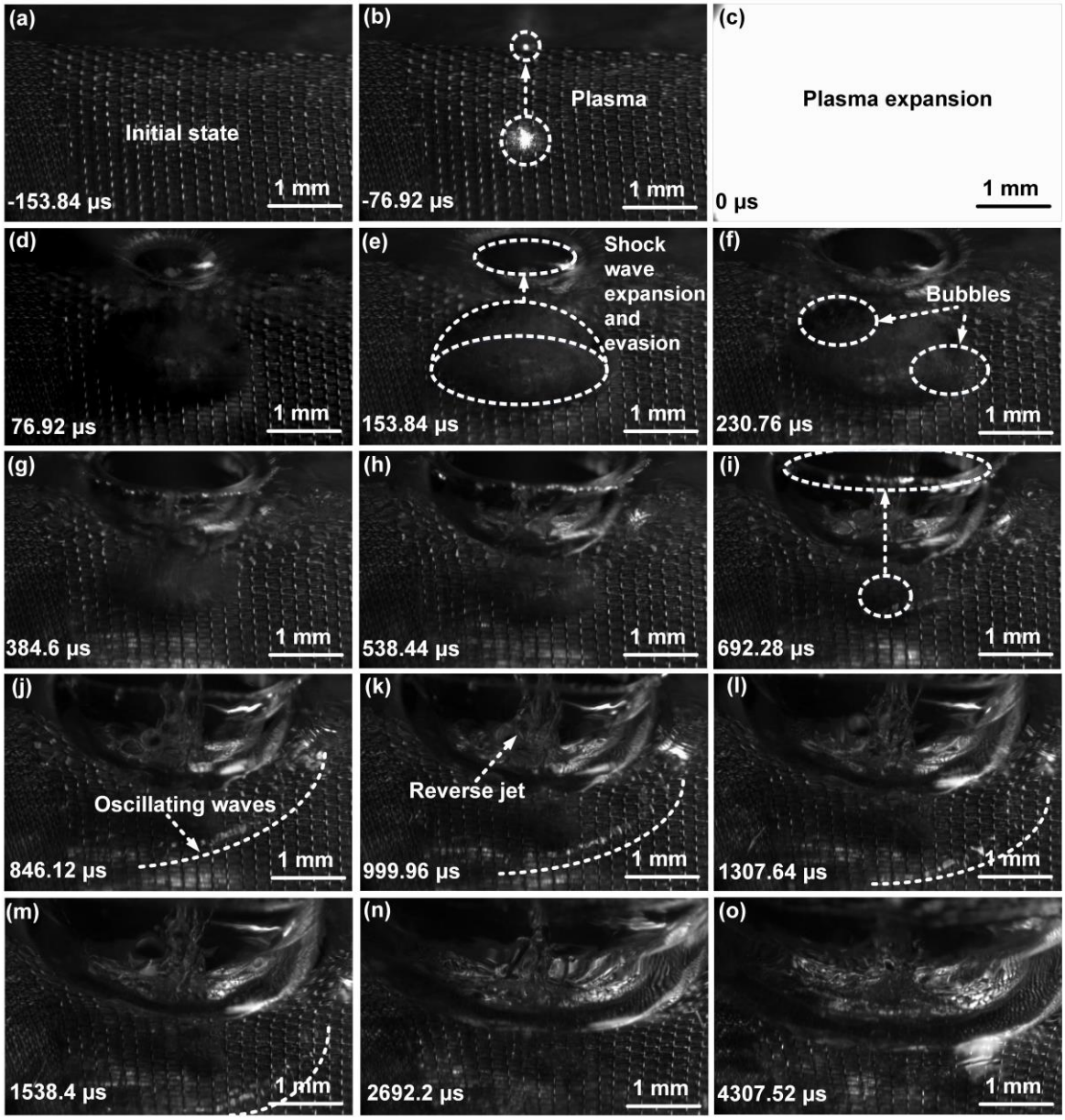

Fig. 7. High-speed camera images of MLSP (the type of metallic mesh is case2): (a) -153.84 μs, (b) -76.92 μs, (c) 0 μs, (d) 76.92 μs, (e)153.84 μs, (f) 230.76 μs, (g) 384.6 μs, (h) 538.44 μs, (i) 692.28 μs, (j) 846.12 μs, (k) 999.96 μs, (l) 1307.64 μs, (m) 1538.4 μs, (n) 2692.2 μs, (o) 4307.52 μs.

4.2. Enhancement mechanisms of mechanical properties of MLSP samples

Here, the strengthening mechanism of the mechanical properties of the structure was described in detail from the perspective of the microstructure and macro mechanics of the materials. The numerical model based on the finite element method was used to provide theoretical support.

Fig. 8 shows the schematic diagram of the enhancement mechanism. When pulsed laser irradiated the surface of aluminum alloy and metal mesh, high temperature plasma and GPa level shock wave would be induced [43]. The surface material was rapidly melted and solidified, which produced a recast layer with rich microstructures on the aluminum alloy surface without metal mesh (**Fig. 2** (h)-**Fig. 2** (i)). Due to the confinement of deionized water, shock wave

expansion was blocked. The shock waves traveled along the thickness of the material. When the shock wave pressure exceeded the dynamic yield limit of the material, the material would produce permanent plastic deformation. Fabbro formula [44] was used to calculate the peak pressure of shock wave, as shown in Equation 1:

$$P_{\max} = 0.01\sqrt{\frac{\alpha}{2\alpha+3}}\sqrt{Z}\sqrt{I_0} \tag{1}$$

Where $P_{\max}$ was the peak pressure of the shock wave induced by the pulse laser, and α was the interaction efficiency between the laser and the metal target. Z was the resultant acoustic impedance, as shown in Equation 2:

$$\frac{2}{Z} = \frac{1}{Z_{mat}} + \frac{1}{Z_{con}} \tag{2}$$

where Z_{mat} was the shock acoustic impedance of the material, and Z_{con} was the impact acoustic impedance of the confinement layer material. I_0 was the power density of the incident laser, as shown in Equation 3:

$$I_0 = \frac{4E}{\pi d^2 \tau} \tag{3}$$

where E was the single pulse energy of the laser, d was the diameter of the laser spot, and τ was the pulse width of the laser. Through calculation, the peak pressure of MLSP process shock wave can reach 3 GPa ((More modeling details can be found in **Section 8** of **Supplementary Materials**), which was far beyond the dynamic yield limit of the material (**Fig. 3** (c)), so it could produce obvious plastic deformation. Dislocation was the main carrier of plastic deformation of materials. The interaction between the shock wave and the material would generate a large number of defects such as dislocation lines, dislocation entanglements and dislocation cells inside the material, and then induce the generation of subgrains [45,46]. The first stage shock wave generated on the aluminum alloy surface and the second stage shock wave transmitted to the aluminum alloy surface through the metal mesh had different peak energy, which was attributed to the continuous attenuation of the shock energy when transmitted in the thin metal mesh. Similarly, shock waves were also attenuated when they were transmitted inside aluminum alloys. The plastic deformation and grain refinement of different parts of the material were not the same with different shock energy. Under the influence of shock waves, more ultrafine grains (UFGs) were generated in the hard phase area without metal mesh coverage, and more fine grains (FGs) were distributed in the sub-hard phase area with metal mesh coverage. The soft phase area not affected by the shock wave retains the original coarse grains (CGs). According to the Hall-Page theory, within a certain grain size range, as the grain size of the material decreased, the microhardness tends to increase [47]. Therefore, the hardness of MLSP samples presented multi-level gradient distribution in the vertical and horizontal directions.

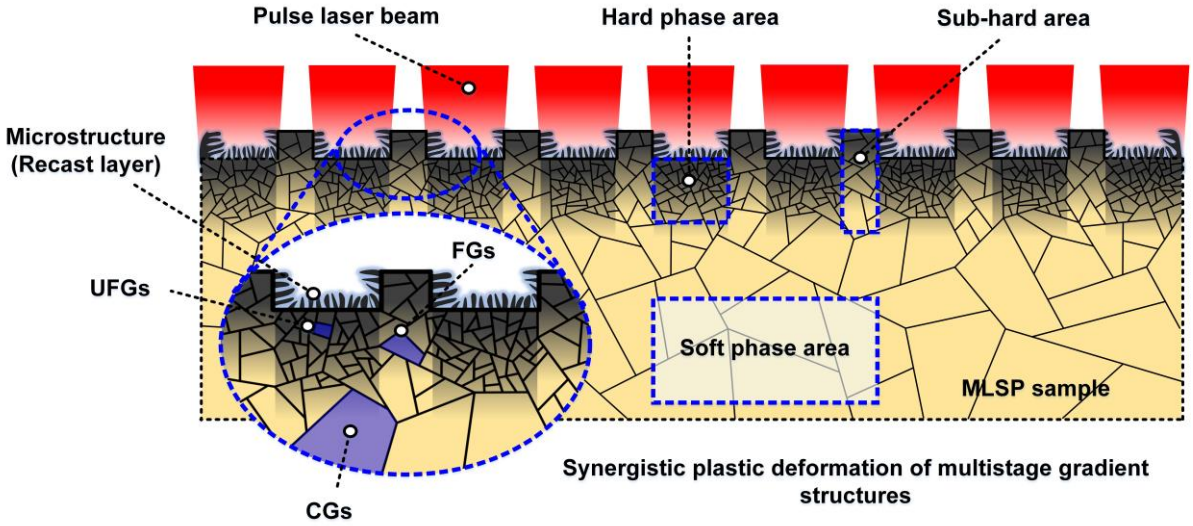

Fig. 8. Schematic diagram of the enhancement mechanism.

Heterogeneous gradient structure was expected to achieve better tensile properties [48,49]. Compared with the single gradient structure generated by the traditional laser shock process, the multi-stage gradient structure induced by MLSP had higher feasibility in improving the tensile properties of materials. In the tensile test, there was a large plastic strain gradient in the hard phase, sub-hard phase and soft phase of MLSP samples and at their junctions. This strain gradient needed to be accommodated by geometrically necessary dislocations (GNDs) .Back stress from geometrically necessary dislocations was used to generate work hardening, preventing premature necking and significantly improving material strength with little sacrifice of material ductility [50]. The distribution of the soft and hard phases of the material was closely related to the tensile properties of the material. Additional uniform tensile stress perpendicular to the tensile direction could be introduced by adding the hard phase structure with alternating regular distribution to the soft phase substrate, which could also effectively avoid early necking and obtain better ductility, which could be shown by the finite element simulation results. As shown in **Fig. 9** (*t* was the tensile fracture time of the sample), the numerical models of all soft phase, alternating soft and hard phases, and all hard phase was established. The ductility of the all soft phase, sample was the largest, followed by the alternating soft and hard phases sample, and the all hard phase sample was the smallest, which was undoubtedly consistent with the ductility change trend of the samples obtained from the real tensile test.

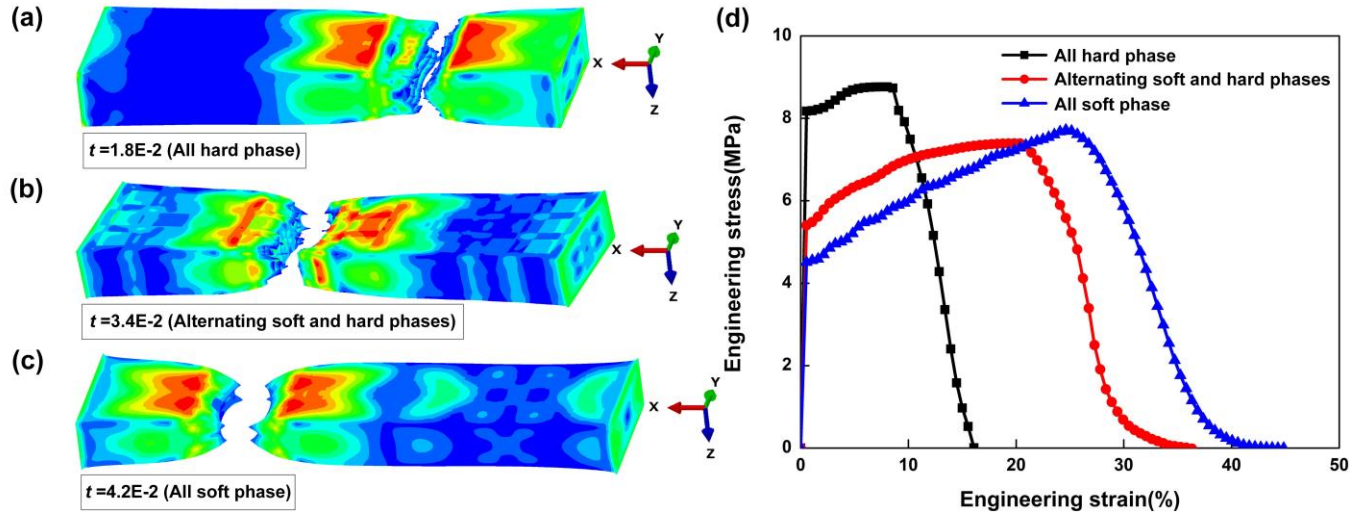

Fig. 9. Tensile simulation results of materials with different structures: (a) all hard phase, (b) alternating soft and hard phases, (c) alternating soft phases, (d) stress-strain curves.

The hardness was related to residual stress [51,52]. In general, residual compressive stress increased hardness. The XRD data could reflect the residual stress state of the sample. **Fig. 10** shows the XRD diffraction patterns of samples produced by different processes. By amplifying the diffraction peak corresponding to the (111) crystal plane locally, it was found that the drift and full width at half maximum (FWHM) of diffraction peak corresponding to the samples produced by different processes were different. Compared with the NLSP sample, the diffraction peaks of the ALSP sample and the MLSP sample were shifted to higher angles. The ALSP sample had the largest offset and the largest FWHM, and the MLSP sample had the second largest in the offset and FWHM. For the MLSP sample, with the increase of the mesh size of the metal mesh, the shift of the diffraction peaks increased, and the FWHM increased. The microscopic residual stress of the material was the main reason for the drift and broadening of the diffraction peaks. The residual compressive stress generated by laser shock would make the interplanar spacing of the material smaller, the diffraction peak would shift to a high angle, and the FWHM would increase [53].

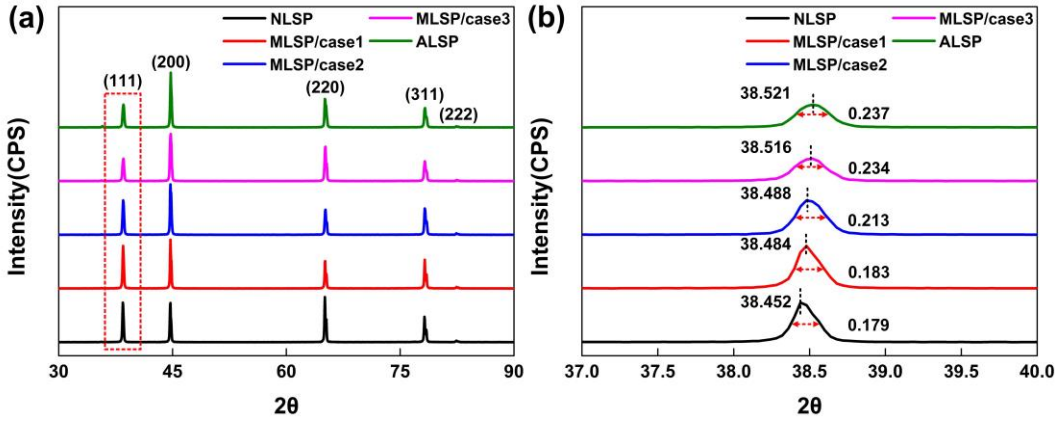

Fig. 10. XRD diffraction patterns of samples produced by different processes: (a) overall picture, (b) partial enlarged view of the (111) crystal plane.

The numerical simulation could predict the effect of structure size on residual stress from macroscopic scale. **Fig. 11** (a)-(h) shows the residual stress and deformation of samples produced by different processes (positive values represented residual tensile stress and negative values represented residual compressive stress). For MLSP samples, the stress distribution state of the substrate area directly irradiated by the pulse laser beam through the metallic mesh was obvious residual compressive stress. Compared with other areas of the substrate, the area of the substrate directly irradiated by the pulse laser beam through the metallic mesh had a higher deformation amount. For ALSP samples, there were relatively uniform residual compressive stress and deformation on the surface of the sample. The stress and deformation curves of the monitoring path could provided more intuitive data for analyzing the stress and deformation of samples. **Fig. 11** (i)-(j) shows the stress-deformation distribution of monitoring paths in samples (the monitoring path is the dotted line). With the increase of the size of the mesh, the peak residual compressive stress and the peak deformation amount of the substrate gradually increased. The peak residual compressive stress and deformation of the ALSP and MSLP samples were similar, which was well consistent with the hardness distribution of the sample in **Fig**. 3 (a).

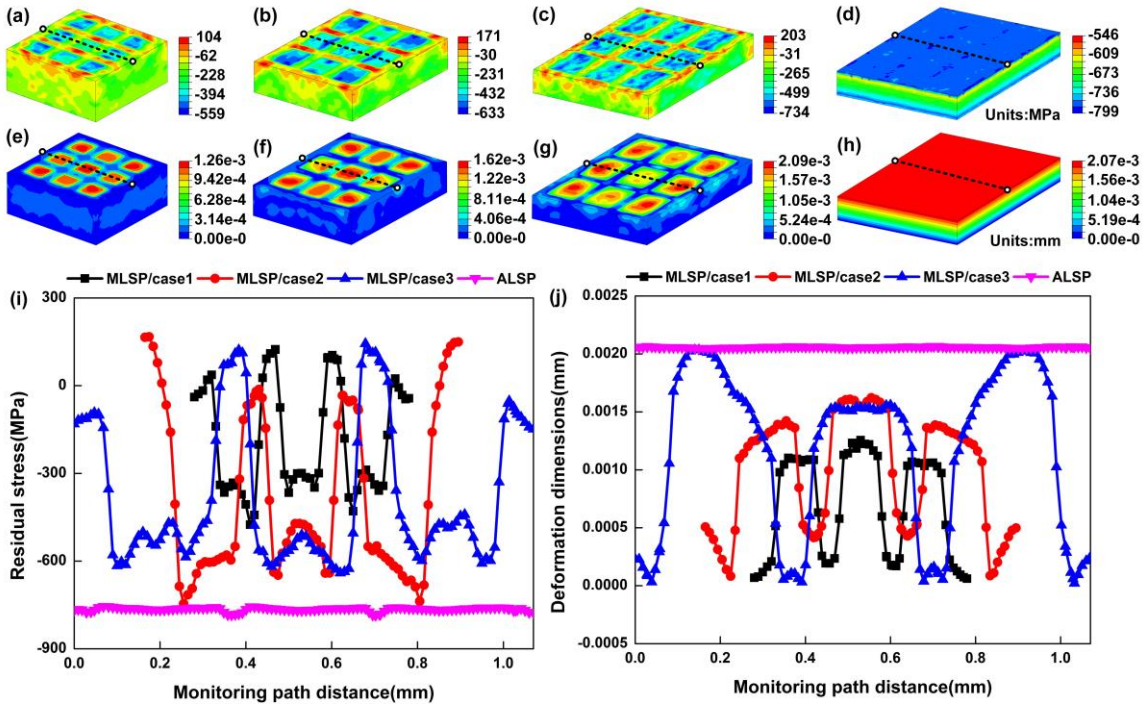

Fig. 11. Residual stress and deformation of samples produced by different processes: (a) MLSP/case1/stress, (b) MLSP/case2/stress, (c) MLSP/case3/stress, (d) ALSP/stress, (e) MLSP/case1/deformation, (f) MLSP/case2/deformation, (g) MLSP/case3/deformation, (h) ALSP/deformation, (i) residual stress of monitoring path, (j) deformation of monitoring path.

4.3. Mechanisms for the functional properties of MLSP samples

The surface morphology and mechanical properties of the structure were closely related to its functional properties. Here, we systematically discussed and analyzed the influence of surface structure and mechanical properties on the functional properties of MLSP samples.

4.3.1. Hydrophobic mechanism of MLSP samples

The microstructure and chemical composition of the material surface were the main factors affecting its wettability. The high-energy shock wave induced by pulse laser caused plastic deformation on the material surface, and produced micro-pits with array distribution (**Fig. 2** (a)-(c)). At the same time, the interaction between high temperature plasma induced by pulse laser and materials led to melting and solidification of materials, thus producing rich micro nano structures (**Fig. 2** (g)-(i)). Micro-pits and microstructures in pits formed a cross scale micro nano composite structure. These cross scale microstructures could spontaneously form hydrophilic chemical groups. When the sample was immersed in a chemical reagent with low surface energy, the fluoride group with low binding energy would be adsorbed on the surface of the microstructure, and then a chemical reaction would occur, which would change the wettability of the material surface and make the material surface hydrophobic. Compared with ALSP sample, the cross scale microstructure of MLSP sample surface had become a perfect gas storage chamber (**Fig. 8**), further reducing the contact area between liquid and solid, and achieving a more excellent Cassie hydrophobic state [54,55].Therefore, MLSP samples had better hydrophobic properties than ALSP and NLSP samples.

4.3.2. Corrosion resistance mechanism of MLSP samples

The chemical activity of aluminum alloy materials was high, and it was easy to form a dense oxide layer in the room temperature environment. During the electrochemical corrosion experiments, the dense and uniform oxide layer blocked the corrosion reaction. Therefore, the oxide layer on the surface was one of the main factors for the excellent corrosion resistance of the aluminum alloy material, thus forming a recast layer (**Fig. 8**). The high temperature plasma induced by the laser would further increase the degree of oxidation of the material. The oxidized area of the substrate directly interacting with the laser beam was larger than that of the metal mesh-covered substrate (**Fig. S6**). The recast layer induced by the interaction between high-temperature plasma and materials was a uniform solid solution with no β phase precipitation along the grain boundary, which greatly reduced the galvanic coupling effect and thus the early pitting corrosion caused by the electrolyte [28]. In addition, laser shock would increase the dislocation density inside the aluminum alloy material, bred more fine subgrains, and finally achieved grain refinement, which was conducive to cultivating a dense and uniform oxide layer inside [56]. The residual compressive stress induced by laser shock (**Fig. 11)** played a positive role in effectively inhibiting the electrochemical activity of metal atoms. Laser shock increased the roughness of the material surface, which provided a larger oxidized connection area and effectively promotes the growth of the oxide film. Under the action of comprehensive factors, the corrosion resistance of the MLSP sample was improved.

4.3.3. Wear resistance mechanism of MLSP samples

The surface structure and mechanical strength of materials were closely related to their tribological properties [57–59]. Observing and comparing **Fig. 12** (a)-(e), the wear scar of the NLSP sample was wider, followed by the MLSP sample, and the ALSP sample was the narrowest. The wear morphology of the NLSP samples was accompanied by deep furrows and some small spalling pits, which were attributed to the mechanical wear effect of hard abrasive chips on the surface of the original samples. Therefore, the wear of the NLSP samples belonged to the composite wear mechanism of abrasive wear and fatigue wear. The wear morphology of the MLSP samples was also accompanied by the wear morphology of the furrows. However, it was worth noting that the furrows of the MLSP samples were significantly shallower than those of the NLSP samples. In addition, the wear morphologies of the MLSP samples were also accompanied by fine cracks generated after the friction debris filled the micro-dimples. The EDS energy spectrum test results showed that there was also obvious oxidation phenomenon in the wear process (**Fig. S7**). Therefore, the wear mechanism of the MLSP samples belonged to the composite wear mechanism of abrasive wear mainly and oxidative wear as the auxiliary. Only furrow morphology was observed in the wear morphology of the ALSP sample. The EDS

energy spectrum test results also confirmed the existence of oxidation phenomenon (**Fig. S7**). Therefore, the wear mechanism of the ALSP sample was also a composite wear mechanism with abrasive wear as the main component and oxidative wear as the auxiliary.

The NLSP sample had not been strengthened, so its surface mechanical strength was low, and it was easy to wear out. The friction debris produced by the wear process had a serious mechanical effect on the surface of the sample, resulting in deep furrows and fatigue spalling pits (**Fig. 12** (f)). For the ALSP sample, the surface of the sample was strengthened, so the surface hardness and the fatigue performance was improved. The surface of MLSP sample was also strengthened. In addition, many micro-pits had been formed on the surface of MLSP samples. The micro-pits on the surface played the role of enhancing the oil storage capacity on the surface of the friction pair to achieve secondary lubrication. The micro-pits could play the function of accommodating wear debris, thereby further reducing the friction coefficient between the contact surfaces of the friction pair and improving the stability of the friction coefficient (**Fig. 12** (f)) [60,61]. However, the mechanical strength of the material surface was still dominant. Despite the MLSP sample was the result of multistage strengthening, and the strengthening effect of the sample under the metallic mesh was still weaker than that of the area directly under the laser beam. Therefore, the tribological properties of the MLSP sample under the current experimental parameters were weaker than that of the ALSP sample.

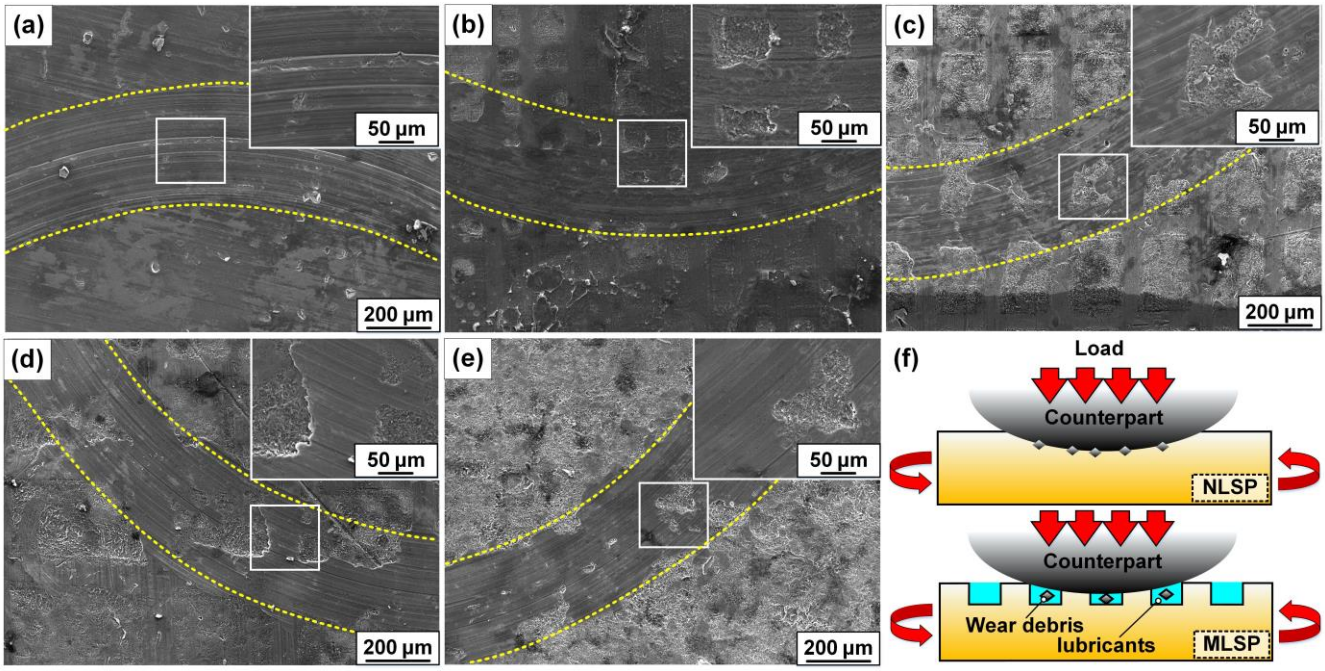

Fig. 12. Wear topography of samples produced by different processes: (a) NLSP, (b) MLSP/case1, (c) MLSP/case2, (d) MLSP/case3, (e) ALSP, (f) schematic diagram of the wear mechanism of the NLSP and MLSP samples.

4.4. Comparison of surface structural properties of different samples

Fig. 13 shows the six dimensional capability radar chart of samples produced by different processes. Here, strength and ductility were used to evaluate the tensile properties of the samples, hardness was used to evaluate the mechanical strength of the samples, contact angle was used to evaluate the hydrophobicity of the samples, corrosion current density was used to evaluate the corrosion tendency of the samples, and friction coefficient was used to evaluate the tribological properties of the samples.

For MLSP samples, high ductility was the highlight of MLSP/case1 samples, structural properties of MLSP/case2 samples were relatively balanced, and high tensile strength and mechanical strength were the highlights of MLSP/case3 samples. High tensile strength and mechanical strength were the highlights of ALSP samples, but the samples had obvious low ductility short plates. On the whole, MLSP had more balanced mechanical and functional properties than NLSP and ALSP samples. In the engineering field, different MLSP treatment processes could be selected according to different application environments. In the future, the surface morphology and mechanical properties of materials could

be further controlled by adjusting the size parameters of metal mesh and laser processing parameters. In addition, in view of the low cost and high ductility of thin metallic mesh, it could be laid on the surface of complex curved structure in a large area. MLSP process could produce functional structures with excellent mechanical strength on the surface of key components in a cheap and efficient way, which was expected to be widely used in aerospace, ocean engineering, locomotive manufacturing and other fields.

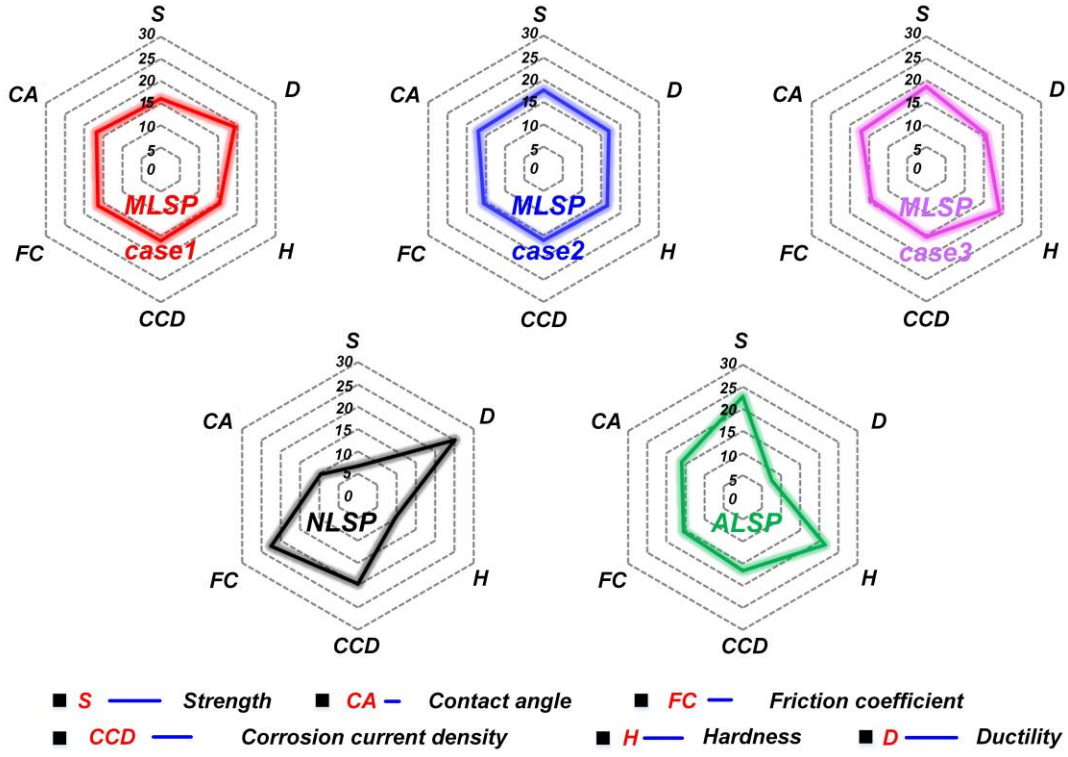

Fig. 13. Six dimensional capability radar chart of samples produced by different processes.

5. Conclusions

The functional surface produced by the conventional process was difficult to overcome the functional-mechanical properties trade-off. In this paper, a strategy called multistage laser shock peening was proposed to one-time fabricate functional microstructure with excellent mechanical properties. The micro morphology, mechanical properties and functional properties of MLSP, NLSP and ALSP samples were systematically analyzed and discussed. The conclusions of this study are as follows:

1) The multistage shock wave induced by pulsed laser produced a multistage heterogeneous gradient structure on the sample surface. The hardness of MLSP samples showed gradient distribution in the horizontal and vertical directions, and the peak hardness increased by 0.55 GPa. Compared with the single gradient structure manufactured by traditional laser shock technology, the multistage gradient structure had more obvious plastic strain gradient, and the work hardening performance of back stress induced by geometric necessary dislocation was more obvious. In addition, the introduction of alternating regularly distributed hard phase regions in the soft phase substrate increased the tensile stress perpendicular to the tensile direction, which could avoid early necking and achieve better cooperative plastic deformation. The yield strength of MLSP samples increased by 214% from 21 MPa to 66 MPa, while the ductility decreased by only 1%.

2) The micro-pits distributed in array on the surface of MLSP sample and the microstructures in the pits constitute the cross-scale composite structure. After the low surface energy treatment, these structures became gas storage chambers, effectively reducing the liquid-solid contact area, resulting in a Cassie hydrophobic surface with a peak contact angle of about 153°.The oxidized recast layer produced by the direct interaction of high temperature plasma induced by pulsed laser with the sample was a uniform solid solution, which greatly reduced the galvanic coupling effect. The residual compressive stress and the refined grain caused by laser shock had positive effects on the electrochemical

activity of metal atoms. The surface of the enhanced MLSP sample showed good tribological properties. The array distributed pit structure could store hard wear debris and lubricants, thus reducing the friction of hard wear debris on the surface. The stored lubricants could also realize secondary lubrication, effectively reducing the friction coefficient.

3) MLSP samples had more balanced mechanical and functional properties than traditional ALSP samples. Different MLSP process strategies could be selected according to the different service environments of the structure to meet the different engineering requirements. By changing the manufacturing method of auxiliary metallic mesh (such as woven mesh, stretched mesh, etc.) and the structural size of metallic mesh (mesh size, mesh shape, etc.), or changing laser process parameters, it was expected to achieve effective adjustment of surface structure and structural properties. The metallic mesh had low cost and good ductility, and could be laid on the surface of curved structure to achieve efficient manufacturing of large area and high reliability functional surfaces. MLSP strategy was expected to play a key role in aerospace, ocean engineering, locomotive manufacturing and other fields.

Acknowledgements

This work was supported by the National Natural Science Foundation of China (Grant No. 51901162). The authors thanked the support of the Chinese National Talent Program.

References

[1] Sun W, Zhu Y, Marceau R, Wang L, Zhang Q, Gao X, et al. Precipitation strengthening of aluminum alloys by room-temperature cyclic plasticity. Science (80-) 2019;363:972–5. https://doi.org/10.1126/science.aav7086.

[2] Wang G, Zhao Y, Hao Y. Friction stir welding of high-strength aerospace aluminum alloy and application in rocket tank manufacturing. J Mater Sci Technol 2018;34:73–91. https://doi.org/10.1016/j.jmst.2017.11.041.

[3] Xiaobo F, Shijian Y. Innovation for forming aluminum alloy thin shells at ultra-low temperature by the dual enhancement effect. Int J Extrem Manuf 2022;4. https://doi.org/10.1088/2631-7990/ac6b62.

[4] Longtin R, Hack E, Neuenschwander J, Janczak-Rusch J. Benign joining of ultrafine grained aerospace aluminum alloys using nanotechnology. Adv Mater 2011;23:5812–6. https://doi.org/10.1002/adma.201103275.

[5] Gayle FW, Goodway M. Aluminum Alloy : The Wright Flyer Crankcase 1994;1788:1992–4.

[6] Wang D, Sun Q, Hokkanen MJ, Zhang C, Lin FY, Liu Q, et al. Design of robust superhydrophobic surfaces. Nature 2020;582:55–9. https://doi.org/10.1038/s41586-020-2331-8.

[7] Fang X, Li Y, Li X, Liu W, Yu X, Yan F, et al. Dynamic Hydrophobic Domains Enable the Fabrication of Mechanically Robust and Highly Elastic Poly(vinyl alcohol)-Based Hydrogels with Excellent Self-Healing Ability. ACS Mater Lett 2020;2:764–70. https://doi.org/10.1021/acsmaterialslett.0c00075.

[8] Hersbach TJP, McCrum IT, Anastasiadou D, Wever R, Calle-Vallejo F, Koper MTM. Alkali Metal Cation Effects in Structuring Pt, Rh, and Au Surfaces through Cathodic Corrosion. ACS Appl Mater Interfaces 2018;10:39363–79. https://doi.org/10.1021/acsami.8b13883.

[9] Saha P, Khedekar K, Wang H, Atanassov P, Cheng L, Stewart S, et al. Correlating the morphological changes to electrochemical performance during carbon corrosion in polymer electrolyte fuel cells. J Mater Chem A 2022;10:12551–62. https://doi.org/10.1039/d2ta02666j.

[10] Bao Y, Fu W, Xu H, Chen Y, Zhang H, Chen S. Bioinspired self-cleaning surface with microflower-like structures constructed by electrochemically corrosion mediated self-assembly. CrystEngComm 2022;24:1085–93. https://doi.org/10.1039/d1ce01267c.

[11] Vargas Garcia JR, Goto T. Thermal barrier coatings produced by chemical vapor deposition. Sci Technol Adv Mater 2003;4:397–402. https://doi.org/10.1016/S1468-6996(03)00048-2.

[12] Šarić I, Kolympadi Markovic M, Peter R, Linić P, Wittine K, Kavre Piltaver I, et al. In-situ multi-step pulsed vapor phase surface functionalization of zirconia nanoparticles via copper-free click chemistry. Appl Surf Sci 2021;539. https://doi.org/10.1016/j.apsusc.2020.148254.

[13] Dianat G, Movsesian N, Gupta M. Vapor Deposition of Functional Porous Polymer Membranes. ACS Appl Polym Mater 2020;2:98–104. https://doi.org/10.1021/acsapm.9b01177.

[14] Li L, Feng L, Bai X, Li ZY. Surface characteristics of Ti–6Al–4V alloy by EDM with Cu–SiC composite electrode. Appl Surf Sci 2016;388:546–50. https://doi.org/10.1016/j.apsusc.2015.10.145.

[15] Wang H, Chi G, Wang Y, Yu F, Wang Z. Fabrication of superhydrophobic metallic surface on the electrical discharge machining basement. Appl Surf Sci 2019;478:110–8. https://doi.org/10.1016/j.apsusc.2019.01.102.

[16] Wang H, Chi G, Jia Y, Yu F, Wang Z, Wang Y. A novel combination of electrical discharge machining and electrodeposition for superamphiphobic metallic surface fabrication. Appl Surf Sci 2020;504:144285. https://doi.org/10.1016/j.apsusc.2019.144285.

[17] Bagherifard S, Slawik S, Fernández-Pariente I, Pauly C, Mücklich F, Guagliano M. Nanoscale surface modification of AISI 316L stainless steel by severe shot peening. Mater Des 2016;102:68–77. https://doi.org/10.1016/j.matdes.2016.03.162.

[18] Maleki E, Unal O. Roles of surface coverage increase and re-peening on properties of AISI 1045 carbon steel in conventional and severe shot peening processes. Surfaces and Interfaces 2018;11:82–90. https://doi.org/10.1016/j.surfin.2018.03.003.

[19] Xu Q, Cao Y, Cai J, Yu J, Si C. The influence of ultrasonic shot peening on the surface roughness, microstructure, and mechanical properties of TC2 thin-sheet. J Mater Res Technol 2021;15:384–93. https://doi.org/10.1016/j.jmrt.2021.08.029.

[20] Dalloz N, Le VD, Hebert M, Eles B, Flores Figueroa MA, Hubert C, et al. Anti-Counterfeiting White Light Printed Image Multiplexing by Fast Nanosecond Laser Processing. Adv Mater 2022;34:1–13. https://doi.org/10.1002/adma.202104054.

[21] Pfleging W. Recent progress in laser texturing of battery materials: A review of tuning electrochemical performances, related material development, and prospects for large-scale manufacturing. Int J Extrem Manuf 2021;3. https://doi.org/10.1088/2631-7990/abca84.

[22] Lian Y, Hua Y, Sun J, Wang Q, Chen Z, Wang F, et al. Martensitic transformation in temporally shaped femtosecond laser shock peening 304 steel. Appl Surf Sci 2021;567:150855. https://doi.org/10.1016/j.apsusc.2021.150855.

[23] Bai Y, Wang H, Wang S, Huang Y, Chen Y, Zhang W, et al. Life cycle strengthening of high-strength steels by nanosecond laser shock. Appl Surf Sci 2021;569:151118. https://doi.org/10.1016/j.apsusc.2021.151118.

[24] Liu XQ, Chen QD, Guan KM, Ma ZC, Yu YH, Li QK, et al. Dry-etching-assisted femtosecond laser machining. Laser Photonics Rev 2017;11. https://doi.org/10.1002/lpor.201600115.

[25] Samanta A, Wang Q, Shaw SK, Ding H. Nanostructuring of laser textured surface to achieve superhydrophobicity on engineering metal surface. J Laser Appl 2019;31:022515. https://doi.org/10.2351/1.5096148.

[26] Trdan U, Skarba M, Porro JA, Ocaña JL, Grum J. Application of massive laser shock processing for improvement of mechanical and tribological properties. Surf Coatings Technol 2018;342:1–11. https://doi.org/10.1016/j.surfcoat.2018.02.084.

[27] Wang H, Keller S, Chang Y, Kashaev N, Yan K, Gurevich EL, et al. Effect of laser shock peening without protective coating on the surface mechanical properties of NiTi alloy. J Alloys Compd 2022;896:163011. https://doi.org/10.1016/j.jallcom.2021.163011.

[28] Kaufman J, Racek J, Cieslar M, Minárik P, Steiner MA, Mannava SR, et al. The effect of laser shock peening with and without protective coating on intergranular corrosion of sensitized AA5083. Corros Sci 2022;194. https://doi.org/10.1016/j.corsci.2021.109925.

[29] Shen Z, Zhang L, Li P, Liu H, Liu K, Lin Y, et al. Altering the surface wettability of copper sheet using overlapping laser shock imprinting. Appl Surf Sci 2021;543:148736. https://doi.org/10.1016/j.apsusc.2020.148736.

[30] Lechthaler B, Fox T, Slawik S, Mücklich F. Direct laser interference patterning combined with mask imaging. Opt Laser Technol 2020;123:105918. https://doi.org/10.1016/j.optlastec.2019.105918.

[31] Dai FZ, Lu JZ, Zhang YK, Luo KY, Zhang L, Wang QW, et al. Micro-dent arrays fabricated by a novel net mask laser shock processing on the surface of LY2 aluminum alloy. J Appl Phys 2012;112. https://doi.org/10.1063/1.4740069.

[32] Ye C, Cheng GJ. Scalable patterning on shape memory alloy by laser shock assisted direct imprinting. Appl Surf Sci 2012;258:10042–6. https://doi.org/10.1016/j.apsusc.2012.06.070.

[33] Tong W, Xiong D. Direct laser texturing technique for metal surfaces to achieve superhydrophobicity. Mater Today Phys 2022;23:100651. https://doi.org/10.1016/j.mtphys.2022.100651.

[34] Yuan G, Liu Y, Ngo C-V, Guo C. Rapid fabrication of anti-corrosion and self-healing superhydrophobic aluminum surfaces through environmentally friendly femtosecond laser processing. Opt Express 2020;28:35636. https://doi.org/10.1364/oe.400804.

[35] Pan R, Zhang H, Zhong M. Triple-Scale Superhydrophobic Surface with Excellent Anti-Icing and Icephobic Performance via Ultrafast Laser Hybrid Fabrication. ACS Appl Mater Interfaces 2021;13:1743–53. https://doi.org/10.1021/acsami.0c16259.

[36] Chen X, Han Z, Lu K. Friction and Wear Reduction in Copper with a Gradient Nano-grained Surface Layer. ACS Appl Mater Interfaces 2018;10:13829–38. https://doi.org/10.1021/acsami.8b01205.

[37] Copper N, Fang TH, Li WL, Tao NR, Lu K. Tensile Plasticity in Gradient. Science (80-) 2011;331:1587–90.

[38] Song Y, Hu Y, Zhang Y, Li G, Wang D, Yang Y, et al. Flexible Tri-switchable Wettability Surface for Versatile Droplet Manipulations. ACS Appl Mater Interfaces 2022;14:37248–56. https://doi.org/10.1021/acsami.2c12890.

[39] Guo L, Tang GH, Kumar S. Dynamic Wettability on the Lubricant-Impregnated Surface: From Nucleation to Growth and Coalescence. ACS Appl Mater Interfaces 2020;12:26555–65. https://doi.org/10.1021/acsami.0c03018.

[40] Gu J, Luo C, Lu Z, Ma P, Xu X, Ren X. Bubble dynamic evolution, material strengthening and chemical effect induced by laser cavitation peening. Ultrason Sonochem 2021;72:105441. https://doi.org/10.1016/j.ultsonch.2020.105441.

[41] Brujan EA, Ikeda T, Matsumoto Y. On the pressure of cavitation bubbles. Exp Therm Fluid Sci 2008;32:1188–91. https://doi.org/10.1016/j.expthermflusci.2008.01.006.

[42] Zhang H, Lu Z, Zhang P, Gu J, Luo C, Tong Y, et al. Experimental and numerical investigation of bubble oscillation and jet impact near a solid boundary. Opt Laser Technol 2021;138:106606. https://doi.org/10.1016/j.optlastec.2020.106606.

[43] Wang C, Wang X, Xu Y, Gao Z. Numerical modeling of the confined laser shock peening of the OFHC copper. Int J Mech Sci 2016;108–109:104–14. https://doi.org/10.1016/j.ijmecsci.2016.02.002.

[44] Fabbro R, Fournier J, Ballard P, Devaux D, Virmont J. Physical study of laser-produced plasma in confined geometry. J Appl Phys 1990;68:775–84. https://doi.org/10.1063/1.346783.

[45] Wang JT, Xie L, Luo KY, Tan WS, Cheng L, Chen JF, et al. Improving creep properties of 7075 aluminum alloy by laser shock peening. Surf Coatings Technol 2018;349:725–35. https://doi.org/10.1016/j.surfcoat.2018.06.061.

[46] Dhakal B, Swaroop S. Effect of laser shock peening on mechanical and microstructural aspects of 6061-T6 aluminum alloy. J Mater Process Technol 2020;282:116640. https://doi.org/10.1016/j.jmatprotec.2020.116640.

[47] Liu WH, Wu Y, He JY, Nieh TG, Lu ZP. Grain growth and the Hall-Petch relationship in a high-entropy FeCrNiCoMn alloy. Scr Mater 2013;68:526–9. https://doi.org/10.1016/j.scriptamat.2012.12.002.

[48] Liu Y, Sun J, Fu Y, Xu B, Li B, Xu S, et al. Tuning strength-ductility combination on selective laser melted 316L stainless steel through gradient heterogeneous structure. Addit Manuf 2021;48:102373. https://doi.org/10.1016/j.addma.2021.102373.

[49] Xing J, Yuan F, Wu X. Enhanced quasi-static and dynamic shear properties by heterogeneous gradient and lamella structures in 301 stainless steels. Mater Sci Eng A 2017;680:305–16. https://doi.org/10.1016/j.msea.2016.10.111.

[50] Wu X, Zhu Y. Heterogeneous materials: a new class of materials with unprecedented mechanical properties. Mater Res Lett 2017;5:527–32. https://doi.org/10.1080/21663831.2017.1343208.

[51] Ling L, Long S, Ma Z, Liang X. Numerical Study on the Effects of Equi-biaxial Residual Stress on Mechanical Properties of Nickel Film by Means of Nanoindentation. J Mater Sci Technol 2010;26:1001–5. https://doi.org/10.1016/S1005-0302(10)60164-8.

[52] Ding Y, Chromik RR. Relationship between indentation plastic zone size and residual stresses in plastically deformed Fe. Mater Sci Eng A 2017;696:1–9. https://doi.org/10.1016/j.msea.2017.04.017.

[53] Fu P, Chu R, Xu Z, Ding G, Jiang C. Relation of hardness with FWHM and residual stress of GCr15 steel after shot peening. Appl Surf Sci 2018;431:165–9. https://doi.org/10.1016/j.apsusc.2017.09.136.

[54] Tenjimbayashi M, Samitsu S, Naito M. Simultaneous Detection and Repair of Wetting Defects in Superhydrophobic Coatings via Cassie–Wenzel Transitions of Liquid Marbles. Adv Funct Mater 2019;29:1–8. https://doi.org/10.1002/adfm.201900688.

[55] Tuvshindorj U, Yildirim A, Ozturk FE, Bayindir M. Robust cassie state of wetting in transparent superhydrophobic coatings. ACS Appl Mater Interfaces 2014;6:9680–8. https://doi.org/10.1021/am502117a.

[56] Guo W, Wang H, He G, Peng P, He D, Han G, et al. Comparison of mechanical and corrosion properties of 7050 aluminum alloy after different laser shock peening. Opt Laser Technol 2022;151:108061. https://doi.org/10.1016/j.optlastec.2022.108061.

[57] Bonse J, Höhm S, Koter R, Hartelt M, Spaltmann D, Pentzien S, et al. Tribological performance of sub-100-nm femtosecond laser-induced periodic surface structures on titanium. Appl Surf Sci 2016;374:190–6. https://doi.org/10.1016/j.apsusc.2015.11.019.

[58] Liu D, Zhang Q, Qin Z, Luo Q, Wu Z, Liu L. Tribological performance of surfaces enhanced by texturing and nitrogen implantation. Appl Surf Sci 2016;363:161–7. https://doi.org/10.1016/j.apsusc.2015.11.245.

[59] Kunz C, Bonse J, Spaltmann D, Neumann C, Turchanin A, Bartolomé JF, et al. Tribological performance of metal-reinforced ceramic composites selectively structured with femtosecond laser-induced periodic surface structures. Appl Surf Sci 2020;499:143917. https://doi.org/10.1016/j.apsusc.2019.143917.

[60] Zhang D, Zhao F, Li Y, Li P, Zeng Q, Dong G. Study on tribological properties of multi-layer surface texture on Babbitt alloys surface. Appl Surf Sci 2016;390:540–9. https://doi.org/10.1016/j.apsusc.2016.08.141.

[61] Sedlaček M, Podgornik B, Ramalho A, Česnik D. Influence of geometry and the sequence of surface texturing process on tribological properties. Tribol Int 2017;115:268–73. https://doi.org/10.1016/j.triboint.2017.06.001.